Space-dependent aspects of electron degradation

A. V. Vasenkov
Institute of Thermophysics, Novosibirsk 630090, Russia
(Received 8 June 1999)

Space- and energy-dependent flux densities were computed by a Monte Carlo method of electron degradation for 0.1–3.0 keV incident electrons in argon. These flux densities contain the basic information about the electron degradation process and can be used to calculate a yield for any inelastic state at any spatial position. Numerical results were analytically represented in terms of the recently introduced phenomenological model. It was found that flux densities multiplied by an absorption cross section in argon are approximately the same as flux densities multiplied by an absorption cross section in nitrogen. This feature provides a basis to use an analytical approximation of flux densities from this study for any gas. [S1063-651X(99)08611-0]

PACS number(s): 52.25.−b, 52.65.−y, 87.50.Gi, 98.58.Ay

I. INTRODUCTION

Understanding the basic mechanisms of interaction of charged particles with matter is a significant problem in radiation physics and chemistry, and especially in radiation biology [1]. Charged particles interact with matter, for the most part, by generating fast electrons. These electrons cause the subsequent processes, namely generating secondary electrons and various ionic and excited species in matter. The process of the electron degradation lasts until the initial electrons and all their secondaries and tertiaries are completely degraded in energy. Usually, various products, formed immediately following electron degradation, are very short-lived and cannot be observed by modern experimental methods; thus, a theoretical study is the only available method. The basic information about these products is contained in electron flux as a function of energy and position. The Monte Carlo simulation has proved to be a very good method for calculating this flux. The Monte Carlo method enables one to numerically simulate an experiment instead of solving an equation or system of equations. Monte Carlo computer codes are also relatively easy to write. One disadvantage of the Monte Carlo approach is that it requires large amounts of computer time. Another disadvantage is that simulation results can be communicated only as a great quantity of numerical data or as graphs. Numerical results given in such forms are often not very useful in establishing the general principles of electron degradation. Fundamentally, the problem of characterizing the basic nature of electron degradation process in a fashion which can be utilized to predict the spatial-dependent yields of any state is a rather difficult one. Green and Singhal [2] , in an attempt to solve this problem, developed an analytic representation for the spatial yield spectra in terms of a model containing three simple microplumes. Using this model, a yield for any inelastic state at any position in the medium can be approximately calculated. In studies of Singhal *et al.* [3], Singhal and Green [4], and Green *et al.* [5], this model was employed to obtain analytical representations of spatial yield spectra for various gases. Recent communication [6] reports an approach that yields an analytic representation of the electron flux densities as a function of energy and spatial position. The basic properties of cross sections were used as a basis for construction of this analytic representation. In this work, a recently introduced model was applied to electron degradation in argon. The results are noteworthy in the following respects. (a) Analytical representations were obtained for various terms used in the model. (b) The individual contributions of these terms to flux densities were studied. (c) The phenomenological approach covered a broader range of incident electron energies than previously. In addition, flux densities multiplied by an absorption cross section in argon were compared with flux densities multiplied by an absorption cross section in nitrogen. The obtained agreement provides the opportunity to use the model from this study for any gas. This paper is arranged as follows. The choice of angular inelastic cross sections for Ar and a brief review of numerical procedure are given in Sec. II. Sensitivity study and results of an analytical representation of space- and energy-dependent electron flux densities are presented in Sec. III. The properties of flux densities in argon and nitrogen are discussed in Sec. IV.

II. MODEL DESCRIPTION

A. Cross sections

Energy degradation in this study was simulated assuming that after excitation an atom would be found in a composite optically forbidden state, or in the optically allowed $4s_{3/2}$, $4s'_{1/2}$, $3d_{3/2}$, $3d'_{3/2}$, and a composite of optically allowed states. The M-shell ionization (with threshold $I_M = 15.76$ eV) event and the L-shell ionization (with threshold $I_L = 250.42$ eV) event were considered as well. During an L-shell ionization event, an Auger electron (with kinetic energy $E_A = 218.9$ eV) was assumed to be emitted with 100% efficiency. Cross sections for the above-mentioned processes were calculated using the formulas given in [7,8].

For realistic simulation of electron transport in a gas, not only energy degradation but also scattering of electrons has to be considered accurately. The elastic collisions, which cause the most scattering of electrons, were simulated using angular cross sections presented in a previous paper [8]. Inelastic scattering of electrons in argon was considered very little in the past and most certainly the reason for this was the fact that so little was known about angular inelastic cross sections. In this study the angular inelastic cross sections of

TABLE I. Parameters for argon angular cross section of a composite optically forbidden excitation event.

E	$10^{-5}\varsigma$	τ_1	τ_2	ζ	γ_1	γ_2	β	ϕ_1	ϕ_2
16	100.0	35247.0	0	599525.0	0.118		0.240	−1.291	
20	20.8	8292.0	0	94211.0	0.153		0.162	−0.863	
30	1.22	4466.0	0	3381.0	0.367		0.147	−0.298	
50	0.533	93.5	109.3	194.0	0.0938	0.0695	0.0827	−1.732	−0.629
100	0.224	21.35	50.85	59.21	0.1005	0.0522	0.0966	−1.634	−0.358

Nicoll and Mohr [9], Chutjian and Cartwright [10], and the angular ionization cross sections of Mohr and Nicoll [11] were analytically represented by the following phase function form:

$$P_l(\theta)=\frac{1}{\sigma_a \varsigma(E)}[\sigma_0 \Psi_l^{\mathrm{I}}(E,\theta)+\sigma_a \Psi_l^{\mathrm{II}}(E,\theta)H(E-I_e)], \tag{1}$$

where

$$\Psi^I(E,\theta)^{-1}=K^2(E,\theta)[\mu^2+K^2(E,\theta)]^{2m},$$

$$K^2(E,\theta)=k^2+k'^2-2kk'\cos(\theta),$$

$$\Psi^{\mathrm{II}}(E,\theta)=\sum_{j=1}^{2}\tau_j(E)/\{1+2\gamma_j(E)-\cos[\theta-\phi_j(E)]\}^2 + \zeta(E)/[1+2\beta(E)+\cos(\theta)]^2.$$

Here, $k(E)h/(2\pi m_a)$ and $k_l'(E-I_l)h/(2\pi m_a)$ are the velocities of the incident and scattered electrons, respectively; I_l is the excitation potential of the lth collision, H is a unit-step function; $\sigma_0=1$ cm^2, $\sigma_a=1$ Å^2; subscription l represents the type of collision. The phase function form for each collisional type is normalized to the corresponding total inelastic cross section; thus the integral of the phase function form over the solid angle is equal to 1. The first term (in brackets) in Eq. (1), which represents the small-angle scattering, is the angular distribution obtained by Nicoll and Mohr using simple Born's theory [9]. Nicoll and Mohr used this distribution to represent nitrogen, neon, argon, and mercury vapor angular inelastic cross sections for small angles of scattering. The values of parameters $m=6.7$ and $\mu=2.81$ were obtained in the case of argon from simple rules given by Slater [12]. The second term in Eq. (1) is phenomenologically added to describe the medium-angle and backscatter enhancements for energies below $I_e=100$ eV. This term is a sum of modified screened Rutherford cross sections. The values of parameters $\varsigma,\tau_1,\gamma_1,\phi_1,\tau_2,\gamma_2,\phi_2,\zeta$, and β for typical electron energies are obtained from fitting of Eq. (1) to various empirical data from [9–11]. These parameters for a composite of optically forbidden excitation, a composite of optically allowed excitation, and a composite of ionization cross sections are given in Table I, Table II, and Table III, respectively. Above 100 eV, the parameter ς was found from the following requirement: $\sigma_a\varsigma(E)=[2\pi\sigma_0\int_0^\pi d\theta\sin(\theta)\Psi^I(E,\theta)]$.

B. Overview of numerical procedure

Spatial- and energy-dependent flux densities have been calculated for incident electron energies up to 3 keV by using the Monte Carlo technique presented in [13]. A normalization for the double differential flux density [with respect to the distance (Z) from the injection point and current energy (E)] was chosen in the form

$$\int \Phi(Z,E,E_p)\sigma_i(E)dE\,dZ=1,$$

where E_p is the incident electron energy and σ_i is the ionization cross section. This requirement is useful for calculation of the efficiency for production of any electron state of atoms or molecules and, consequently, initial plasma composition [8]. (By the term ''initial plasma composition'' I mean composition of plasma that is formed immediately following electron collisions and degradation.)

III. RESULTS

A. Sensitivity study

The effect of the L-shell ionization, the Auger effect, and the anisotropic inelastic scattering on the electron energy degradation in argon is the subject of this subsection. The influence of the L-shell ionization and the Auger effect on the electron degradation spectrum $Z(E,E_p)$ have been much investigated by Kimura *et al.* [1] using the Spencer-Fano equation. The electron degradation spectrum $Z(E,E_p)$ (in units of eV^{-1} cm) is related to the flux density $\Phi(E,E_p)$ (in units of eV^{-1} Å^{-2}) by the following equation:

TABLE II. Parameters for argon angular cross section of a composite optically allowed excitation event.

E	$10^{-3}\varsigma$	τ_1	τ_2	ζ	γ_1	γ_2	β	ϕ_1	ϕ_2
16.0	341.0	37.211	0	42166.8	0.0287		0.398	−1.075	
20	244.0	74.951	0	10904.0	0.0352		0.190	−1.002	
30	29.9	6.064	0	141.4	0.0521		0.0944	−1.593	
50	24.0	5.696	24.2	3.966	0.0576	0.0567	0.0369	−1.728	−0.511
100	12.3	1.237	1.378	3.93	0.0492	0.0237	0.0619	−1.647	−0.580

TABLE III. Parameters for argon angular cross section of a composite ionization event.

E	10^{-3}s	τ_1	τ_2	ζ	γ_1	γ_2	β	ϕ_1	ϕ_2
30	12.2	261.0	0	2034	0.614		0.629	−1.488	
40	15.2	395.0	0	2265	0.442		0.731	−1.046	
60	6.67	0.976	54.93	3.474	0.0625	0.423	0.0543	−1.834	−0.555
100	6.59	1.088	3.008	5.12	0.0577	0.054	0.0438	−1.698	−0.656

$$Z(E,E_p)=\frac{N_i(E_p)}{n_g}\Phi(E,E_p),$$

where $N_i(E_p)$ is the cumulative yield of ions and n_g is the gas density. The yield of ions obtained in this study for $E_p=2$ keV is equal to 73.58. This value is less then 1% lower as compared to the yield of ions obtained by Kowari and Inokuti [14]. I compare in Fig. 1 the electron degradation spectrum, generated from flux density results at a total pressure of 1 atm and at a temperature of 0 °C, with the spectrum from [14]. We see that two degradation spectra have the same general features. But the spectrum from this study slightly overestimates the results of Kowari and Inokuti. The major reason for this is attributed to distinctions between the total ionization cross section from this work and the total ionization cross section used by Kowari and Inokuti. In Monte Carlo calculations, the cross section was used that was constructed on the base of assessments of recent experimental data from Heer *et al.* [15], Krishnakumar and Srivastava [16], and Straub *et al.* [17]. This ionization cross section underestimates the ionization cross section of Eggarter and Inokuti [7] (which was used by Kowari and Inokuti) for energies up to 1 keV. The other reasons which cause the distinctions between two spectra are the following: (i) the calculation methods are not the same, (ii) the excitation cross sections of electronic states are not the same, (iii) the emission energy of the Auger electron is not the same. (In the work by Kowari and Inokuti, the Auger electron was emitted with energy equal to 200 eV.)

It is of interest to determine if the inelastic anisotropic scattering affects the spatial energy deposition. To accomplish this, calculations were made by the Monte Carlo method using, first, angular cross sections from Sec. II and, second, the scattering model from a previous study [8]. In the previous scattering model, the following assumptions were used for modeling inelastic collisions. For $E\leqslant 100$ eV, electrons were scattered through optically allowed excitation events according to the elastic angular cross section, while the angular cross section for collisions with excitation of a composite of optically forbidden states was substituted by an angular isotropic scattering function. For energies above 100 eV, it was assumed that the angular deflection on inelastic scattering is negligible. The comparison of results, obtained using different scattering models, revealed no observed difference between the two spatial energy deposition distributions for incident energies above 1 keV. Thus, the effect of anisotropic inelastic scattering on spatial energy deposition is insignificant at high incident electron energies. It was found that anisotropic inelastic scattering affects the spatial energy deposition for incident energies below 1 keV. To illustrate this effect, I show in Fig. 2 the efficiency for the production from a composite of forbidden states, and the combined efficiency, obtained as a sum of the efficiencies for each electronic state, for representative incident energy $E_p=0.1$ keV. The distance along the Z axis is expressed in units of a range R (i.e., a path length that electrons pass as their energy decreases from incident energy to the minimum excitation threshold). Lines represent calculations using angular cross sections from this study; points represent computations using the scattering model from [8]. The efficiency for the production from a composite of forbidden states is shown because

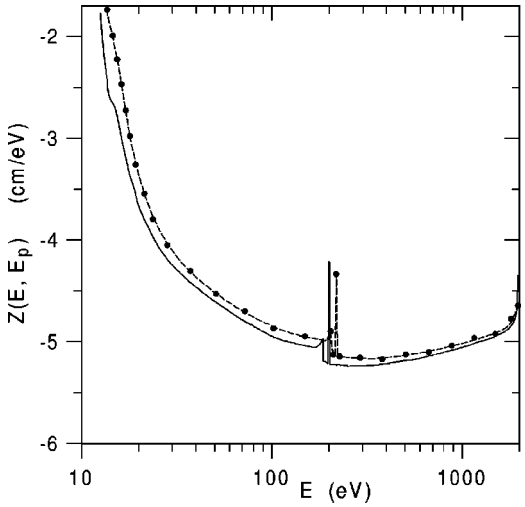

FIG. 1. Electron degradation spectrum $Z(E,E_p)$. Points represent Monte Carlo calculations; dashed line is an approximative curve. Solid line represents results of Kowari and Inokuti [14].

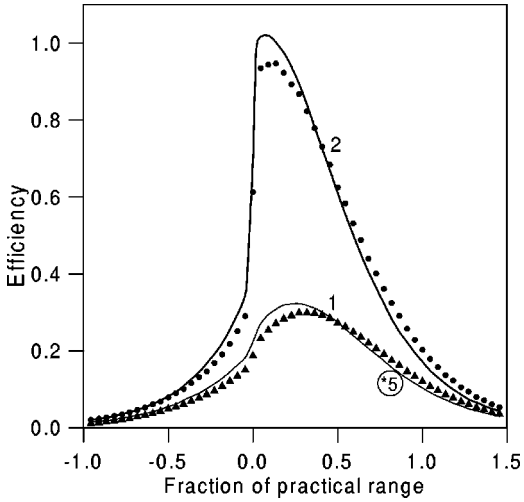

FIG. 2. Efficiency for production of a composite forbidden state (1) and a combined efficiency obtained as a sum of the efficiencies for each electronic state (2): lines represent calculations using angular cross sections from this study, points represent computations using scattering model from previous work [8].

TABLE IV. Range data (in 10^{-6} g/cm^2) at selected incident energies (in keV). I and II: results obtained using correspondingly a set of cross sections presented in Sec. II and that from a previous study [8].

E_p	R_0^{I}	R_0^{II}
0.1	0.6	0.7
0.5	3.8	3.8
1	9.0	9.6
2	25.1	27.1
3	49.3	54.2

the energy dependence for the cross section of excitation of a composite of forbidden states is clearly different from that for other inelastic cross sections. Figure 2 shows that changes in efficiency for the production from a composite of forbidden states, and combined efficiency, which results from the change in the scattering model, are similar in a qualitative sense. These changes can be summarized as follows. Near the injection point in calculations using angular cross sections from this study, electrons deposit more energy than electrons in computations using the scattering model from [8]. This is because the present scattering model causes more electron scattering than does the scattering model from the previous work. Away from the injection point, calculations using the present scattering model predict less energy deposited as compared to that calculated using the scattering model from [8]. This change in energy deposition reflects, in part, the renormalization of the distribution to account for the change in the energy deposition near the injection point. The energy deposition behind the injection point is because of backscattered electrons. We see that the present scattering model yields more energy deposited as compared to that calculated using the model from the previous study. This points to the conclusion that the present inelastic scattering model causes more backscattering of electrons than does the previous model.

The energy deposition plots are often used to calculate a range for electrons [18]. The ranges from our previous work are compared with those obtained in this study in Table IV. We see that R_0^{II} differs from R_0^{I} by errors varying from 2% to 15%. The changes for $E_p<1$ keV mainly result from the change in the anisotropic inelastic scattering model. For higher incident energies the changes are predominantly due to the effect of the L-shell ionization event, and the Auger effect was taken into account in the present calculations.

B. Energy deposition

Spatial distribution of the energy deposition rate is an important characteristic, because it provides a rough idea on the physics of the spatial deposition of energy. Following the results of Green and Singhal [8] and Vasenkov [8], I represented the longitudinal distribution of the energy deposition rate obtained in this study by

$$\Psi(z,E_p)=[a_0(E_p)]^{-1}\exp\left\{\sum_{i=0}^{2} a_i(E_p)z^i\right\}, \qquad (2)$$

where $z=Z/R_a$, $R_a=10^{-6}(0.85+7.85E_p^{1.65})$g/cm^2, and values of the parameters are given in Table V. The integral of $\Psi(z)$ over z is equal to 1. The energy deposition plots generated from Monte Carlo calculations are shown in Fig. 3. The abscissa in the figure is the reduced depth. The calculation results are compared with Eq. (2) for three representative incident energies. We see that the quality of the fits is improved as the incident energy increases. This is because, in a low-energy range, first, inelastic cross sections do not follow the Born-Bethe approximation and each have its individual dependence on energy, and, second, differential elastic cross section structure is rather complex.

TABLE V. Parameters used in Eq. (2). Incident energy in keV.

Parameter	$0.1<E_p<0.5$	$0.5\leqslant E_p\leqslant 1.5$	$1.5<E_p<2.5$	$E_p\geqslant 2.5$
a_0	0.84	0.79	1.04	1.09
a_0	-0.078	-0.088	-1.30×10^{-5}	-0.0021
a_1	1.21	1.12	2.23	3.04
a_2	-3.03	-3.03	-4.02	-4.44

C. Analytical representation of electron flux densities in a high-energy range

Considering the properties of flux densities, it is useful to start with construction of their analytical representation in a high-energy range [6]. The three-dimensional flux densities in this range can be represented by (in units of eV^{-1}Å^{-2})

$$\Phi^{\mathrm{II}}(z,E,E_p)\Psi(z,E_p)^{-1} = \Lambda(E_p)\left(1+\sum_{l=0}^{1}\psi_l(E_p)z^l\delta(E-E_A)\right) \times\left\{\left(\sum_{l=0}^{2}G_l(z,E/E_p,E_p)^{-1}\right)^{-1}+\exp(\varphi(z))[\Gamma(z,E_p) - E/E_p]^{-\eta(z)}H(z)\right\}^{-1}, \qquad (3)$$

$$G_l(z,E/E_p,E_p)^{-1}=[\exp(\Xi_l(z))(E/E_p)^{\beta_l(z)} \times H(\overline{z_l}-z)]/\Theta(z,E/E_p,E_p), \qquad (4)$$

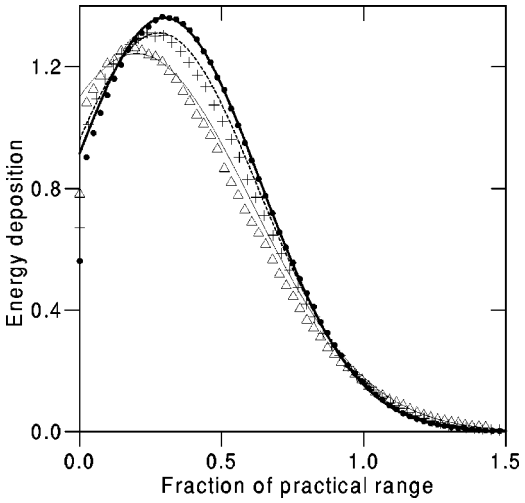

FIG. 3. Energy deposition: points represent Monte Carlo calculation, lines represent the analytic fit using Eq. (2); (△), $E_p=0.3$ keV; (+), $E_p=2.0$ keV; (●), $E_p=3.0$ keV.

$$\Theta(z,E/E_p,E_p) = \begin{cases} \tilde{\alpha}(E_p) & \text{for } E/E_p < \epsilon(E_p) \\ \ln(\tilde{\beta}(z)E/E_p) & \text{for } E/E_p \geq \epsilon(E_p). \end{cases} \quad (5)$$

Here H is a unit-step function equal to 0 at the argument of a function less than or equal to 0. Current and incident energies are in units of 1 keV. The parameter expressions for Eqs. (3)–(5) are given in Appendix A for incident energies below 3 keV. For higher incident energies it is necessary to set $\Lambda=\Lambda(3)$, $\Theta=\Theta(z,E/3,3)$, and $G_0=G_0(z,E/3)$; the other parameter expressions are determined as given by Appendix A. This requirement reflects the fact that energy deposition curves are practically identical for incident energies above 3 keV [8]. Including unit-step functions (with $\overline{z_0}=1.0$, $\overline{z_1}=0.70$, $\overline{z_2}=0.25$) in the first term (in curly brackets) on the right-hand side of Eq. (3) reflects the drastic changes of flux densities with the distance from the injection point. The second term represents flux densities at energies close to the incident energy. A unit-step function in this term is used to consider the fact that a high-energy part of the flux density at $z=0$ is formed mainly by a contribution from the source. $\Gamma(z,E_p)=\xi+\Sigma_{k=1}^{2}\Delta_k(z)z^kE_p$ is incorporated in the second term to take into account the decrease in energy of primary electrons with the increase of distance from the injection point. By primary electrons, I mean incident electrons that scattered or degraded in energy. I should note that for $E>\epsilon(E_p)$, the first term of Eq. (3) depends on energy via the ratio E/E_p. The second term, which represents flux densities at energies close to the incident energy, is dependent on energy via two variables E/E_p and E_p, but the dependence of this term on incident energy is rather weak. The contribution of Auger electrons to a flux density is represented by including the Dirac δ function. This contribution increases with incident energy.

A comparison of Eq. (3) with Monte Carlo data is shown in Figs. 4(a) and 4(b) for two incident energies and four longitudinal values. Lines are used to represent contributions given by $G_0(z,E/E_p,E_p)$ (dash lines), $1/\Sigma_{l=0}^{1}G_l(z,E/E_p,E_p)^{-1}$ (dash-dot lines), $1/\Sigma_{l=0}^{2}G_l(z,E/E_p,E_p)^{-1}$ (dash-dot-dot lines), and the second term (in curly brackets) on the right-hand side of Eq. (3) (solid lines). The thick solid lines represent the total contribution. Monte Carlo data are shown by points. The flux densities given in Figs. 4(a) and 4(b) are quantitatively rather different, but the general features of $\Phi^{\mathrm{II}}(z,E,E_p)$ are practically unaffected by the change in incident energy. We see that at $z=0$ the contribution of $G_0(z,E/E_p)$ is superior to the contributions from other terms for energies below $0.85E_p$. The flux densities weakly vary with energy for this energy range. For higher energies the contributions from all terms of a sum given by Eq. (4) are considered to describe the rapid increase of flux densities with energy. At $z=0.2$ the contribution of $G_0(z,E/E_p)$ dominates the contributions from other terms for energies below $0.45E_p$. The flux densities are represented by a balance between the first and second term of Eq. (3) for the energy range wherein flux densities reach the maximum. The second term of Eq. (3) is used to describe the flux densities at about the incident energy. Flux densities exhibit simpler properties at larger distances from the injection point. This is because with the increase of distance the energy spectrum of the flux densities has few high-energy electrons. As a result, the first term of Eq. (3) takes a simpler form. For $z=0.4$, the contribution of this term is determined by contributions of the first two terms of a sum given by Eq. (4) in the whole energy range considered. For $z=0.9$, the first term of Eq. (3) is equal to $G_0(z,E/E_p)$.

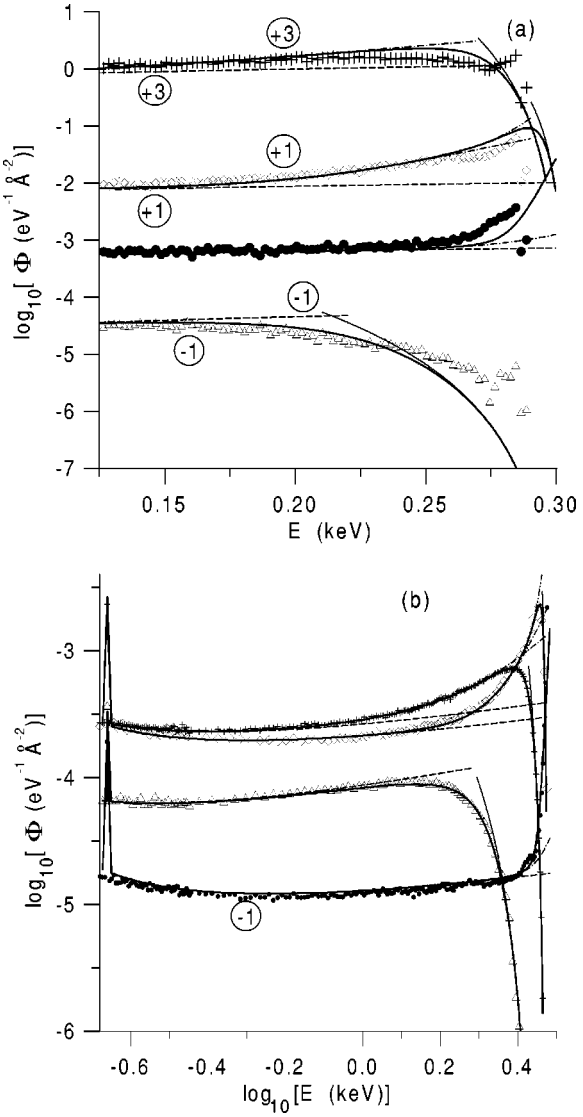

FIG. 4. High energy parts of electron flux densities vs current energy at two incident energies and three distances to the injection point: (a) $E_p=0.3$ keV, $R_0=1.9\times10^{-6}$ g/cm^2; (b) $E_p=3.0$ keV, $R_0=49.3\times10^{-6}$ g/cm^2. The Monte Carlo calculations are represented by symbols: (●), $z=0$; (◇), $z=0.2$; (+), $z=0.4$; (△), $z=0.9$. The analytic fits are represented by lines; see text for details.

D. Analytical representation of electron flux densities in a whole range

Following the recent communication of Vasenkov [6], the analytical representation of flux densities as a function of position, current, and incident energies is given by

$$\Phi(z,E,E_p)=\Phi^{\mathrm{I}}(z,E,E_p)+\Phi^{\mathrm{II}}(z,E,E_p). \quad (6)$$

Here, the first term represents the low-energy parts of the

flux densities:

$$\Phi^{\mathrm{I}}(z,E,E_p)=\Psi(z,E_p)\left\{\sum_{i=0}^{1}\exp[A_i(E_p)]\times E^{-|\alpha_i(E_p)|}H(E_A-W^*-E)\right\}, \qquad (7)$$

where W^* is the first excitation potential of argon. The parameter expressions for Eq. (7) are given in Appendix B for incident energies below 3 keV. For higher incident energies it should be set $\Phi^{\mathrm{I}}=\Phi^{\mathrm{I}}(z,E,3)$. I should stress that independence of low-energy parts of flux densities from high incident energy is not a special feature of electron distribution formation in argon but can be attributed to basic properties of electron degradation in a gas. The low-energy electron distribution is basically formed by secondary electrons of different generations. These electrons are produced by ionization. As a result, the energy of a secondary electron is practically independent of the incident energy.

The results of fitting Eq. (6) to Monte Carlo data are shown in Figs. 5(a), 5(b), and 5(c). The contributions of the first and second terms of a sum given by Eq. (7) are shown by dash and dash-dot lines, respectively. We see that the first term of this sum contributes at energies about excitation potentials of electronic states of Ar. The contribution from the second term prevails over the contribution from the first term for higher energies. Flux densities obtained for different incident energies at the injection point are shown in Fig. 5(a). We see that a form of flux density becomes more complex with the increase of incident energy. This is because the L -shell ionization event and the Auger effect play an important role in electron degradation at high incident energies. At $z=0.5$, forms of flux densities near the incident energy are rather different from those shown in Fig. 5(a). Flux densities slightly increase as the energy approaches E_p. Then, flux densities drop rapidly just before the incident energy. For the flux densities shown in Fig. 5(c), the energy range can be conveniently divided into three intervals. In a low-energy range, flux densities decrease as the energy arises. For higher energies but lower than the incident energy, flux densities weakly vary with energy. Flux densities drop rapidly just before the incident energy.

To elucidate the possibilities of the proposed model, I show in Fig. 6 the analytical representation of flux densities for $E_p=2$ keV. We see that the calculated three-dimensional surface is a complex structure. General features in $\Phi(z,E,E_p)$ can be summarized as follows. At about the incident energy, the number of high-energy electrons tends to diminish as the distance from the injection point increases. We see a peak at 219 eV (because of the Auger effect) and a complex structure below the peak. The magnitude of the peak decreases with the increase of distance. In a low-energy range, $\Phi(z,E,E_p)$ increases with energy. This is because of a contribution from secondary electrons.

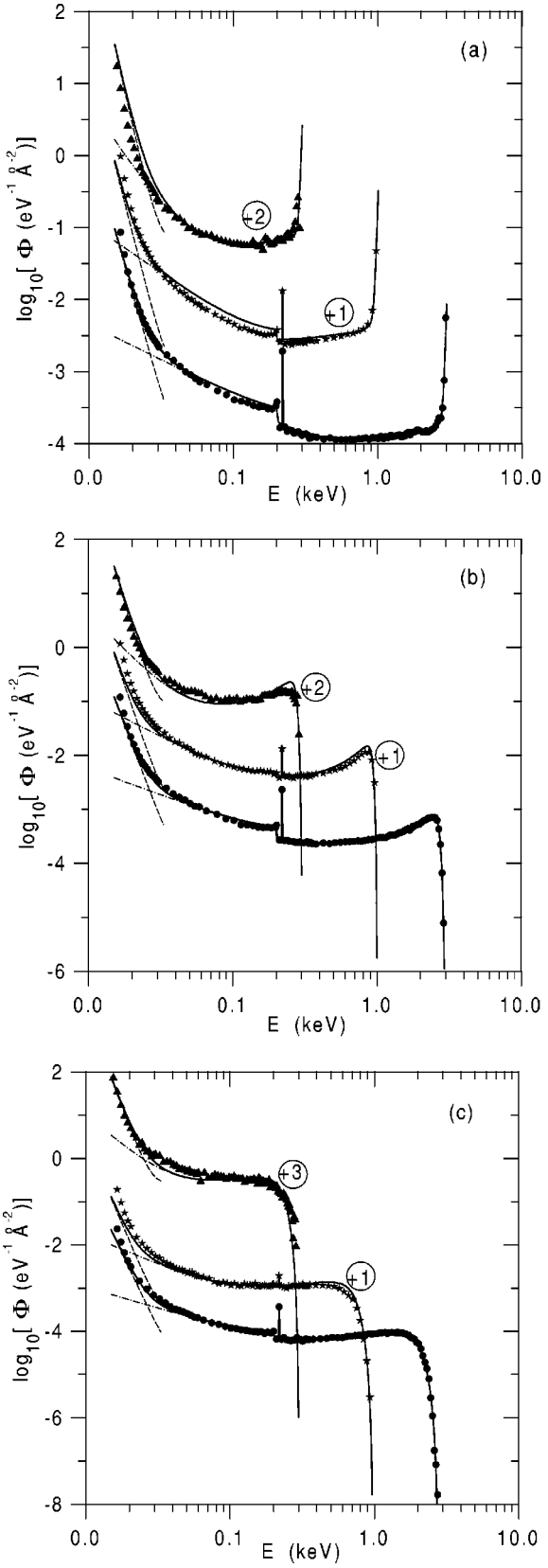

FIG. 5. Electron flux densities vs current energy at three incident energies and three distances to the injection point: (a) $z=0$; (b) $z=0.4$; (c) $z=0.9$. Points represent Monte Carlo calculations: (triangles), $E_p=0.3$ keV, $R_0=1.9\times10^{-6}$ g/cm^2; (stars), $E_p=1.0$ keV, $R_0=9.0\times10^{-6}$ g/cm^2; (circles), $E_p=3.0$ keV, $R_0=49.3\times10^{-6}$ g/cm^2. Lines represent analytical fits; see text for details.

IV. DISCUSSION AND CONCLUSIONS

The space- and energy-dependent flux densities were calculated in this work using a Monte Carlo method for incident

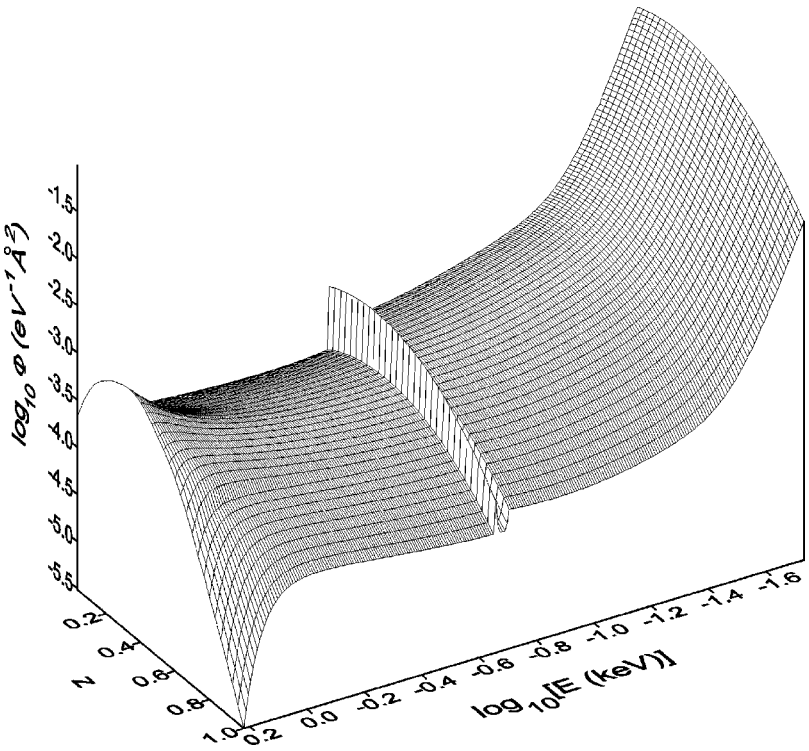

FIG. 6. Analytical representation of electron flux densities vs current energy and distance to the injection point at representative incident energy equal to 2 keV, $R_0 = 25.1 \times 10^{-6}$ g/cm^2.

electrons of energy 0.1–3.0 keV in argon. Electron energy degradation and both elastic and inelastic scattering were considered in this simulation. The integral and differential cross sections used for modeling these processes were in agreement with measurements. Numerical flux density results were analytically represented in terms of the recently introduced phenomenological model. This model can be successfully used for other gases as well. The fundamental reason for this hypothesis is in the nature of electron-atom and electron-molecule cross sections. Green and Singhal [2] were probably the first to note that the individual inelastic cross sections divided by the total inelastic cross section and the differential elastic cross sections divided by the total elastic cross section are fairly similar from one species to another within the energy range of interest.

In support of the versatility of the proposed model, I compared flux densities in argon and nitrogen. Flux densities in nitrogen were calculated by the Monte Carlo method of electron degradation using the inelastic cross sections by Porter *et al.* [19], the ionization cross sections by Jackman *et al.* [20], and the total and differential elastic cross sections by Porter *et al.* [18]. Flux densities multiplied by an absorption cross section in argon are compared with flux densities multiplied by an absorption cross section in nitrogen in Fig. 7. Results are shown for three longitudinal values at representative incident energy equal to 1 keV. Ranges for electrons were calculated from Eq. (11) of [8] . We see that the calculated distributions are rather similar in the two gases. The considerable differences are visible only at energies below 50 eV. There are two basic reasons for these disagreements. First, the Born-Bethe formula does not govern the inelastic cross sections in a low-energy range. Hence, each cross section has its individual dependence on energy. Second, angular cross sections in argon and nitrogen are rather distinctive at low energies. It is of interest to discuss separately the reason why curves differ at energies about thresholds of electronic excitations. In this energy range, electrons effectively lose energy during optically forbidden excitations in nitrogen. The effect of optically forbidden excitations on energy deposition in argon is of lesser significance. As a result, $\Phi\sigma_A$ decreases with energy in nitrogen and increases as the energy decreases in argon.

Nitrogen and argon represent a typical atomic and molecular system. Hence, the approximate invariance of flux densities multiplied by an absorption cross section in argon and nitrogen provides the opportunity to use an analytical approximation of flux densities from this study for any gas.

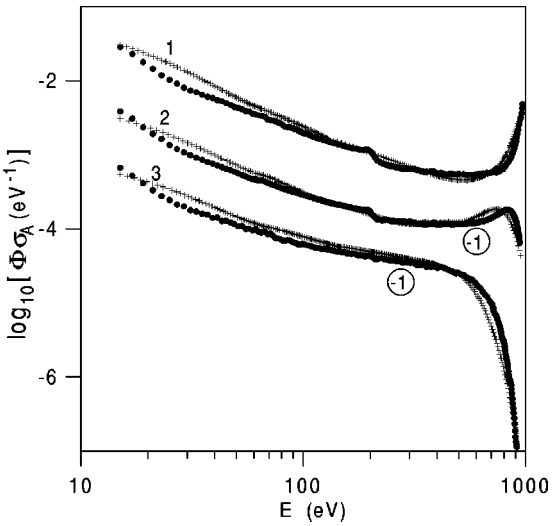

FIG. 7. Flux densities multiplied by an absorption cross section in argon ($R_0 = 9 \times 10^{-6}$ g/cm^2) are compared with flux densities multiplied by an absorption cross section in nitrogen ($R_0 = 6 \times 10^{-6}$ g/cm^2) at representative incident energy equal to 1 keV: (1), $z = 0.1$; (2), $z = 0.4$; (3), $z = 1.0$.

TABLE VI. Parameters used for analytical representation of electron flux densities in a high-energy range.

Parameter	Value	Parameter	Value
		$\tilde{h}_1^6$	-3464
Scale factors		$\tilde{h}_2^0$	-4.541
		$\tilde{h}_2^1$	34.30
$\tilde{\lambda}_1$	1.803	$\tilde{h}_2^2$	-285.8
$\tilde{\lambda}_2$	0.557	$\tilde{h}_2^3$	635
		M_0	3
Parameters used to represent		M_1	4
contribution of Auger electrons		M_2	3
		$\tilde{f}_0^0$	0.676
E_*	0.36	$\tilde{f}_0^1$	0.0
$\tilde{d}_0^0$	-2.799	$\tilde{f}_0^2$	0.193
$\tilde{d}_0^1$	8.282	$\tilde{f}_1^0$	16.68
$\tilde{d}_0^2$	-1.264	$\tilde{f}_1^1$	-60.46
$\tilde{d}_1^0$	2.123	$\tilde{f}_1^2$	95.39
$\tilde{d}_1^1$	-6.842	$\tilde{f}_1^3$	-54.78
$\tilde{d}_1^2$	1.274	$\tilde{f}_2^0$	67.81
		$\tilde{f}_2^1$	-240.0
Parameters used in first term		$\tilde{f}_2^2$	355.3
(in curly brackets) of Eq. (3)			
		Parameters used in second term	
$\tilde{g}_0$	0.0443	(in curly brackets) of Eq. (3)	
$\tilde{g}_1$	-0.0297		
$\tilde{g}_2$	0.0154	$\tilde{q}_0$	-4.743
N_0	2	$\tilde{q}_1$	4.511
N_1	7	$\tilde{q}_2$	12.36
N_2	4	$\tilde{q}_3$	-8.918
$\tilde{h}_0^0$	-7.496	ξ	1.011
$\tilde{h}_0^1$	1.527	Δ_1	-0.00212
$\tilde{h}_1^0$	-9.624	Δ_2	-0.0293
$\tilde{h}_1^1$	93.76	$\tilde{u}_0$	0.436
$\tilde{h}_1^2$	-788.8	$\tilde{u}_1$	15.72
$\tilde{h}_1^3$	3299	$\tilde{u}_2$	-27.01
$\tilde{h}_1^4$	-7281	$\tilde{u}_3$	19.38
$\tilde{h}_1^5$	8017	$\tilde{u}_3$	-4.857

ACKNOWLEDGMENTS

This research was supported by the Russian State Program for Support of the Integration of Education and Science for 1997–2000 under Contract No. 274.

APPENDIX A: ANALYTIC EXPRESSIONS USED IN EQS. (3)–(5)

In this appendix, I present the parameter expressions used to construct the analytical representation of flux densities in a high-energy range. Scale factor $\Lambda(E_p)$ from Eq. (3) is chosen to be equal to $\tilde{\lambda}_1 E_p^{-\tilde{\lambda}_2}$. The Auger electron contribution is represented by a sum of polynomials in E_p,

TABLE VII. Parameters used for analytical representation of electron flux densities in a low-energy range.

Parameter	Value	Parameter	Value
Parameters used in second term of Eq. (7)		Parameters used in first term of Eq. (7)	
χ_0	-42.04	ϱ_0^0	-22.09
χ_1	7.58	ϱ_1^0	23.74
χ_2	-1.23	ϱ_2^0	-12.74
		ϱ_0^1	-11.65
		ϱ_1^1	0.558

$$\psi_l(E_p)=\sum_{k=0}^{2}\tilde{d}_l^k E_p^k H(E_p-E_*).$$

Here, a step function is used to consider the fact that the contribution of Auger electrons is negligible for incident energies below E_*.

Functions $\Xi_l(z)$ and $\beta_l(z)$ from Eq. (4) are represented by polynomials in z:

$$\Xi_l(z)=\sum_{k=0}^{N_l-1}\tilde{h}_l^k z^k,$$

$$\beta_l(z)=\sum_{k=0}^{M_l-1}\tilde{f}_l^k z^k.$$

Functions $\tilde{\alpha}(E_p)$ and $\epsilon(E_p)$ from Eq. (5) are given by simple equations:

$$\tilde{\alpha}(E_p)=\begin{cases}1 & \text{for } 2<E_p<1\\ 3-E_p, & \text{for } 1\leqslant E_p\leqslant 2,\end{cases}$$

$$\epsilon(E_p)=\begin{cases}0 & \text{for } E_p<1\\ 0.2/E_p & \text{for } E_p\geqslant 1.\end{cases}$$

The dependence of $\tilde{\beta}(z)$ on z is determined by

$$\tilde{\beta}(z)=\left(\sum_{k=0}^{2}\tilde{g}_k z^k\right)^{-1}.$$

Functions $\varphi(z)$ and $\eta(z)$, used in the second term (in curly brackets) on the right side of Eq. (3), are given by

$$\varphi(z)=\sum_{k=0}^{3}\tilde{q}_k z^k,$$

$$\eta(z)=\sum_{k=0}^{4}\tilde{u}_k z^k.$$

Coefficients for presented formulas are summarized in Table VI.

APPENDIX B: ANALYTIC EXPRESSIONS USED IN EQ. (7)

In a low-energy range the flux densities are represented using the following four functions: $A_0(E_p)$, $A_1(E_p)$, $\alpha_0(E_p)$, and $\alpha_1(E_p)$. The functions $A_0(E_p)$ and $A_1(E_p)$ are dependent on incident energy in a complicated way. It was found that it is useful to divide the energy range for $A_0(E_p)$ into three intervals:

$$A_0(E_p)=\begin{cases} -38.55 \ \text{ for } \ E_p\leqslant 0.5 \\ \sum_{k=0}^{2} (\chi_k E_p^k) \ \text{ for } \ 0.5<E_p<2 \\ -31.80 \ \text{ for } \ E_p\geqslant 2. \end{cases}$$

In a similar way the energy range for $A_1(E_p)$ was divided into two intervals:

$$A_1(E_p)=\begin{cases} \sum_{k=0}^{2} (\varrho_k^0 E_p^k) \ \text{ for } \ E_p\leqslant 1 \\ \sum_{k=0}^{1} (\varrho_k^1 E_p^k) \ \text{ for } \ E_p>1. \end{cases}$$

The functions $\alpha_0(E_p)$ and $\alpha_1(E_p)$ are smoothly dependent on incident energy:

$$\alpha_0(E_p)=\exp[-1.103\ln(E_p)+2.061]E_p,$$

$$\alpha_1(E_p)=0.6/E_p+0.8.$$

Coefficients for the formulas given here are summarized in Table VII.

[1] M. Kimura, M. Inokuti, and M. A. Dillon, in *Advances in Chemical Physics*, edited by I. Prigogine and S. A. Rice (Wiley, New York, 1993), Vol. 84, p. 193.

[2] A. E. S. Green and R. P. Singhal, Geophys. Res. Lett. **6**, 625 (1979).

[3] R. P. Singhal, C. H. Jackman, and A. E. S. Green, J. Geophys. Res. A **85**, 1246 (1980).

[4] R. P. Singhal and A. E. S. Green, J. Geophys. Res. A **86**, 4776 (1981).

[5] A. E. S. Green, Dayashankar, P. F. Schippnick, D. E. Rio, and J. M. Schwartz, Radiat. Res. **104**, 1 (1985).

[6] A. V. Vasenkov, Phys. Rev. E **59**, R4773 (1999).

[7] E. Eggarter and M. Inokuti, Argonne National Laboratory Radiological and Environmental Research Division Report, 1980, ANL-80-58, p. 29.

[8] A. V. Vasenkov, Phys. Rev. E **57**, 2212 (1998).

[9] F. H. Nicoll and C. B. O. Mohr, Proc. R. Soc. London, Ser. A **142**, 320 (1933).

[10] A. Chutjian and D. C. Cartwright, Phys. Rev. A **23**, 2178 (1981).

[11] C. B. O. Mohr and F. N. Nicoll, Proc. R. Soc. London, Ser. A **144**, 596 (1934).

[12] J. C. Slater, Phys. Rev. **36**, 57 (1927).

[13] A. V. Vasenkov, Ph. D. dissertation, Institute of Thermophysics, Novosibirsk, 1996 (unpublished).

[14] K. Kowari and M. Inokuti, Phys. Rev. A **42**, 795 (1990).

[15] F. J. de Heer, R. H. J. Jansen, and W. van der Kaay, J. Phys. B **12**, 979 (1979).

[16] E. Krishnakumar and S. K. Srivastava, J. Phys. B **21**, 1055 (1988).

[17] H. S. Straub, P. Renault, B. G. Lindsay, K. A. Smith, and R. F. Stebbings, Phys. Rev. A **52**, 1115 (1995).

[18] H. S. Porter, F. Varosi, and H. G. Mayr, J. Geophys. Res. A **92**, 5933 (1987).

[19] H. S. Porter, C. H. Jackman, and A. E. S. Green, J. Chem. Phys. **65**, 154 (1976).

[20] C. H. Jackman, R. H. Garvey, and A. E. S. Green, J. Geophys. Res. **82**, 5081 (1977).